Linear spectral numerical model for internal gravity wave propagation

Julien Marty, Francis Dalaudier

Linear Spectral Numerical Model for Internal Gravity Wave Propagation

J. MARTY

CEA, DAM, DIF, Arpajon, France

F. DALAUDIER

CNRS/INSU, LATMOS/IPSL, Université Versailles St-Quentin, and UPMC-Paris 6, Paris, France

(Manuscript received 19 June 2009, in final form 23 October 2009)

ABSTRACT

A three-dimensional linear spectral numerical model is proposed to simulate the propagation of internal gravity wave fluctuations in a stably stratified atmosphere. The model is developed to get first-order estimations of gravity wave fluctuations produced by identified sources. It is based on the solutions of the linearized fundamental fluid equations and uses the fully compressible dispersion relation for inertia–gravity waves. The spectral implementation excludes situations involving spatial variations of buoyancy frequency or background wind. However, density stratification variations are taken into account in the calculation of fluctuation amplitudes. In addition to gravity wave packet free propagation, the model handles both impulsive and continuous sources. It can account for spatial and temporal variations of the sources, encompassing a broad range of physical situations. The method is validated with a monochromatic pressure monopole, which is known to generate St. Andrew's cross–shaped waves. It is then applied to the case of the ozone layer cooling during a total solar eclipse. The asymptotic response to a Gaussian thermal forcing traveling at constant velocity and the transient response to the 4 December 2002 eclipse show good agreement with previous numerical simulations. Further applications for the model are discussed.

1. Introduction

The French Atomic Energy Commission (CEA) has performed various measurement campaigns of atmospheric pressure fluctuations using very sensitive (10^{-3} Pa) ground-based microbarograph networks. Among recorded pressure fluctuations, gravity wave events have been identified. Previous gravity wave measurement campaigns (e.g., Hauf et al. 1996; Rees et al. 2000) have shown that it is not easy to determine gravity wave packet characteristics from ground pressure signals and even harder to identify their sources. This was one motivation for constructing a simple numerical model able to simulate ground pressure fluctuations generated by gravity wave propagation. Several gravity wave propagation models have already been proposed. Some have studied theoretical situations such as the response to an oscillating source moving through the atmosphere, including an analytical model based on Green's function (Voisin 1994) or a numerical spectral model based on the determination of eigenfunctions through the ray approximation (Broutman and Rottman 2004). Others have been applied to more realistic situations such as jet streams (Fritts and Luo 1992), convection (Fovell et al. 1992), topography (Broutman et al. 2003), or total solar eclipses (Fritts and Luo 1993).

In this paper, we present a three-dimensional linear spectral numerical model that can propagate internal gravity wave fluctuations in a stably stratified atmosphere. Rather than solving the linearized fundamental fluid equations with source terms, the present model simply implements the free propagation of the *unforced* solutions—namely, monochromatic internal gravity waves. The influence of the source terms is time discretized and handled as impulsive modification of the solutions. Thus, the model can account for spatial and temporal evolution of both source and wave field. All calculations are performed in the spectral domain using the numerical convenience of the three-dimensional discrete Fourier transform (3D-DFT). The objectives of the model are manifold. First, it must provide first-order estimations of gravity wave fluctuations generated by identified sources

Corresponding author address: J. Marty, CEA, DAM, DIF, F-91297 Arpajon, France.
E-mail: julien.marty@cea.fr

DOI: 10.1175/2009JAS3237.1

(explosions, solar eclipse, etc.). Synthetic fluctuations produced by the model can then be compared to observations and facilitate measurement campaign planning. The model must also help characterize the pressure signature of gravity wave packets in microbarograph records. Ground pressure synthetic signals can be used to test signal processing methods devoted to gravity wave detection and characterization.

The model is based on the gravity wave *linear* theory for a stably stratified atmosphere, which has often shown a good ability to describe the first-order behavior of gravity waves (Fritts and Alexander 2003). Each wave is treated independently, as if it were the only one present in the system. Superposition of several monochromatic gravity waves accounts for wave packets but waves cannot interact to exchange energy. Thus, processes such as wave breaking, wave–mean flow interactions, or wave–wave interactions are discarded, as well as all the resulting energy transfers. Solutions of linearized equations must then be viewed as estimations useful for interpreting observations rather than accurate results. The method is presented for the fully compressible gravity wave dispersion relation (e.g., Marks and Eckermann 1995; Fritts and Alexander 2003). It can, however, take into account other gravity wave dispersion relations resulting from approximations of the fully compressible one.

Since the propagation occurs in the spectral domain, the atmospheric parameters of the gravity wave dispersion relation are not allowed to vary. Spatial variations of the buoyancy frequency N, the background wind $(\overline{u}, \overline{v}, 0)$, and the density scale height H are therefore excluded. A constant buoyancy frequency removes any possible reflection or ducting cases. A spatially uniform background wind prevents the analysis of some gravity wave sources such as jet streams. However, we will see in section 4a that it allows us to easily take into account gravity wave sources with constant velocity by working in the source reference frame. The density scale height is an important parameter in the dispersion relation for long vertical wavelengths, but its influence on the calculation of wave amplitudes is even more essential. This is particularly true at high altitude as wave amplitude exponentially increases with height. To obtain more realistic results, we will show that while keeping the density scale height constant in the gravity wave dispersion relation, it is possible to take into account any given atmospheric density profile for the calculation of wave amplitudes.

Despite some limitations, we will see that this model encompasses a broad range of physical situations. Its design makes it simple to use and to understand. The method is described in section 2, including the handling of impulsive and continuous sources. The model is validated in section 3 with a monochromatic Gaussian monopole, which is known to generate St. Andrew's cross–shaped waves (e.g., Lighthill 1978; Voisin 1991). In section 4, it is applied to the case of the ozone layer cooling during a solar eclipse, which generates large-scale gravity waves (Chimonas and Hines 1970). The asymptotic solution is compared to Chimonas' (1970) analytical theory and Fritts and Luo's (1993) numerical solutions. The transient response to the 4 December 2002 eclipse is also investigated. Our solutions show good agreement with results obtained by Eckermann et al. (2007), who used a high-altitude global numerical weather prediction model. Finally, some future applications for the model are discussed in section 5.

2. Model description

a. Linear theory solutions

We refer to the review of Fritts and Alexander (2003) for the linearization in Cartesian coordinates (x, y, z) of fundamental fluid equations around a horizontally uniform hydrostatic basic state with background wind $(\overline{u}, \overline{v}, 0)$, potential temperature $\overline{\theta}$, density $\overline{\rho}$, and pressure $\overline{p}$ varying only in z. By assuming the (angular) buoyancy frequency N and the background wind to be spatially uniform, we obtain a set of equations with *exact* solutions, which can be expressed as a linear superposition of monochromatic waves of the form

$$\left(u', v', w', \frac{\theta'}{\overline{\theta}}, \frac{p'}{\overline{\rho}}, \frac{\rho'}{\overline{\rho}}\right) = (\tilde{u}, \tilde{v}, \tilde{w}, \tilde{\theta}, \tilde{p}, \tilde{\rho}) \times \exp\left[i(kx + ly + mz - \omega t) + \frac{z}{2H}\right]. \quad (1)$$

Here H is the density scale height and $(u', v', w', \theta'/\overline{\theta}, p'/\overline{\rho}, \rho'/\overline{\rho})$ a perturbation induced by a monochromatic gravity wave with wave vector $\mathbf{k}$ [components (k, l, m)] and Eulerian angular frequency ω, which can be written as

$$\omega = \hat{\omega} + k\overline{u} + l\overline{v}. \quad (2)$$

The intrinsic angular frequency $\hat{\omega}$ represents the angular frequency that would be observed in a reference frame moving at the background wind velocity. It is solution of a biquadratic equation [Fritts and Alexander 2003, their Eq. (22)] that has two separated families of solutions, one related to acoustic–gravity waves and the other to inertia–gravity waves. We here focus on the second family of solutions, whose dispersion relation reads

$$\hat{\omega}^2 = \frac{Bc_S^2}{2}\left(1 - \sqrt{1 - \frac{4A}{B^2 c_S^2}}\right), \tag{3}$$

with

$$A = N^2(k^2 + l^2) + f^2\left(m^2 + \frac{1}{4H^2}\right), \tag{4}$$

$$B = k^2 + l^2 + m^2 + \frac{1}{4H^2} + \frac{f^2}{c_S^2}, \tag{5}$$

where c_S represents the sound speed and f the Coriolis parameter, assumed to be constant over a considered region. This dispersion relation has even solutions $(\hat{\omega}, \mathbf{k})$ and $(-\hat{\omega}, -\mathbf{k})$, which are physically identical. Thus, we follow the usual sign convention and only retain $(\hat{\omega}, \mathbf{k})$ solutions where $\hat{\omega}$ is positive. We note that this dispersion relation simultaneously takes into account buoyancy N, density stratification H, compressibility c_S, and rotational f effects. Depending on the wave vector range, some terms can be neglected to simplify the analysis. The only term that is always insignificant is the last term in Eq. (5) as $1/4H^2 \gg f^2/c_S^2$. For real-valued wave vector components (k, l, m), the intrinsic angular frequency $\hat{\omega}$ is bounded between the Coriolis parameter f and the buoyancy frequency N. We now define the normalized pressure fluctuation ϕ' as

$$\phi'(x, y, z, t) = p'(x, y, z, t)\frac{\rho_0}{\overline{\rho}(z)}e^{-z/2H}, \tag{6}$$

with $\rho_0 = \overline{\rho}(0)$ being the density at the ground. According to Eq. (1), the normalized pressure fluctuation ϕ' can be decomposed into a linear superposition of monochromatic gravity waves $\phi'_{k,l,m}$ with *constant* amplitudes $\tilde{\phi}_{k,l,m} = \rho_0 \tilde{p}_{k,l,m}$ over the whole spatial domain:

$$\phi'_{k,l,m}(x, y, z, t) = \tilde{\phi}_{k,l,m} e^{i(kx+ly+mz-\omega t)}. \tag{7}$$

The model is mainly developed to help interpret microbarographs records. Thus, influence of ground reflection on pressure variation must be taken into account. Reflection of internal waves has been intensely studied in both the atmosphere and the ocean (e.g., Thorpe 1987). We here simplify the problem by considering a horizontal ground surface. We start from Fritts and Alexander [2003, their Eqs. (15)–(20)] to deduce the polarization relation between complex amplitudes $\tilde{p}$ and $\tilde{w}$ of the gravity wave perturbation:

$$\tilde{p} = -\frac{N^2 - \hat{\omega}^2}{\hat{\omega}(m - i\Gamma)}\tilde{w}, \tag{8}$$

with Γ, the wavenumber, defined as

$$\Gamma = \frac{g}{c_S^2} - \frac{1}{2H}. \tag{9}$$

It is sometimes referred to as the Eckart coefficient (Gossard and Hooke 1975). We assume that the reflection is total in the sense that the energy of the incident and reflected wave is conserved. As usual, the boundary conditions at the ground are vertical velocity vanishing and angular frequency conservation:

$$\tilde{w}_i = -\tilde{w}_r, \quad \omega_i = \omega_r, \tag{10}$$

with the subscripts i and r respectively related to the incident and reflected waves. It follows that

$$k_i = k_r, \quad l_i = l_r, \quad m_i = -m_r. \tag{11}$$

From Eq. (8) we deduce the normalized pressure fluctuation amplitude $\tilde{\phi}_r$ of the reflected wave:

$$\tilde{\phi}_r = \tilde{\phi}_i\left(\frac{m_i - i\Gamma}{m_i + i\Gamma}\right). \tag{12}$$

The complex amplitude of the normalized pressure fluctuation undergoes a phase shift when the wave reflects. However, this phase shift does not exceed 10° for vertical wavelengths less than 10 km and atmospheric parameters with standard tropospheric or stratospheric values.

b. Free temporal evolution

In the following sections, the method will be described for the pressure because it is the variable recorded by microbarographs. However, complex amplitudes of wave perturbation variables described in Eq. (1) are linked together by polarization relations and therefore can be retrieved from the pressure variation. A complex-valued normalized pressure fluctuation field [Eq. (6)] is taken as initial state for the time $t = 0$. This field can be expressed by its spectral components using the three-dimensional inverse discrete Fourier transform (3D-IDFT):

$$\phi'(x, y, z, 0) = \sum_{k,l,m} \hat{\phi}_{k,l,m} e^{i(kx+ly+mz)}, \tag{13}$$

with $\hat{\phi}$ the 3D-DFT of the normalized pressure fluctuation field ϕ' at the time $t = 0$. By comparing Eq. (13) with Eq. (7), we can identify the Fourier coefficients $\hat{\phi}_{k,l,m}$ with the normalized pressure fluctuation amplitudes $\tilde{\phi}_{k,l,m}$ of the monochromatic gravity waves. In the case of a real-valued initial field, we will see in section 2d that directions

of propagation can be specified by applying a filtering operation in the spectral domain. It can be seen from Eq. (3) that the angular frequency only depends on wave vector components when the buoyancy frequency, the density scale height, and the background wind are spatially constant. Thus, as long as no source interferes, the normalized pressure fluctuation field $\phi'(x, y, z, 0)$ can be propagated over any arbitrary time interval t by shifting the phase of its Fourier coefficients with the appropriate angular frequency $\omega(k, l, m)$:

$$\phi'(x, y, z, t) = \sum_{k,l,m} (\hat{\phi}_{k,l,m} e^{-i\omega t}) e^{i(kx+ly+mz)}. \quad (14)$$

The modulus of spectral components always remains the same. Only the phase varies and is responsible for the temporal evolution. The wave field after propagation is complex even in the case of real-valued initial wave field. Its imaginary part $\mathrm{Im}[\phi'(x, y, z, t)]$ can be interpreted as the Hilbert transform of its real part $\mathrm{Re}[\phi'(x, y, z, t)]$ up to an overall sign. This is because we have chosen complex exponential solutions to resolve linearized fundamental fluid equations (Bracewell 1999). It is an interesting characteristic of the model that provides not only the real part of the wave field but also its phase. It can be useful for signal processing methods based on the Hilbert transform such as the calculation of signal instantaneous frequency or phase and group velocities. Here we refer to the definition of the Hilbert transform as associating the imaginary part of the analytical signal to its real part. Finally, the pressure fluctuation field p' can be deduced at any altitude from the normalized pressure fluctuation field ϕ' by rearranging Eq. (6) into

$$p'(x, y, z, t) = \phi'(x, y, z, t) \sqrt{\frac{\overline{\rho}(z)}{\rho_0}}, \quad (15)$$

where the exponential variation of the density with the altitude has been replaced by the square root of density ratio in order to better account for energy conservation. This allows us to take into account a realistic atmospheric density profile when calculating the pressure fluctuation even though the density scale height has been assumed to be constant in the dispersion relation.

c. Source effects

Free temporal propagation can be used for any time interval as long as no source of pressure fluctuations interferes with the medium. When a source starts modifying the pressure field, its effects must be taken into account before propagating the wave field further. If the source duration is small with respect to $2\pi/N$ (period corresponding to the buoyancy frequency), the source can be considered as impulsive. The total effect of the source on the normalized pressure fluctuation field is added instantaneously and the free temporal propagation method described above can be applied to propagate the new wave field. The model can therefore be used to investigate cases such as explosions, which quasi-instantaneously modify the pressure field. Nevertheless, most gravity wave sources cannot be considered impulsive (convection, topography, solar eclipses, etc.) and source effects need to be time discretized. We here consider a normalized pressure fluctuation forcing (per unit time) F_ϕ. This forcing term can be decomposed into a series of impulsive elements s_n representing the integration of the source effects on the normalized pressure fluctuation field around the time t_n:

$$s_n(x, y, z) = \int_{t_n-(t_n-t_{n-1})/2}^{t_n+(t_{n+1}-t_n)/2} F_\phi(x, y, z, t)\, dt. \quad (16)$$

Because of the linearity of the model, we can successively add each source effect sample such that

$$\hat{\phi}_{k,l,m}(t_n) = [\hat{s}_{n-1} + \hat{\phi}_{k,l,m}(t_{n-1})] e^{-2i\pi(\omega/\omega_{Sn})}. \quad (17)$$

Here $\hat{\phi}_{k,l,m}(t_{n-1})$ is the 3D-DFT of the normalized pressure field, just before taking into account the effects of the source around the time t_{n-1}; $\hat{s}_{n-1}$ is the 3D-DFT of the source effect sample s_{n-1} and ω_{Sn} is the instantaneous angular sampling frequency between the time t_{n-1} and t_n, defined as

$$\omega_{Sn} = \frac{2\pi}{t_n - t_{n-1}}. \quad (18)$$

This sampling frequency is not necessarily constant but must be chosen carefully. First, the *temporal* Nyquist criterion needs to be satisfied so that the effects of the source on the normalized pressure fluctuation field are properly represented. Second, waves generated by a succession of impulsive source effect samples but not produced by the corresponding continuous source can appear. These unwanted waves are directly linked to the choice of the sampling frequency and can be eliminated by always keeping the sampling frequency outside of the frequency propagation domain:

$$\omega_{Sn} > \omega(k_N, l_N, m_N) + \mathbf{k}_N \cdot \mathbf{u}_S, \quad (19)$$

with (k_N, l_N, m_N) being the components of the *spatial grid* Nyquist wave vector $\mathbf{k}_N$ and $\mathbf{u}_S$ the source velocity.

In the case of zero background wind and for a stationary source, the internal gravity wave frequency domain is bounded from above by the buoyancy frequency. Thus, a sufficient condition for (19) is

$$\omega_{Sn} > N. \tag{20}$$

The consequences of violating this condition will be demonstrated in section 3 with a monochromatic Gaussian monopole time discretized with a frequency lower than the buoyancy frequency. This characteristic would make it more difficult to take into account the propagation of acoustic–gravity waves from continuous sources within this model. This would indeed require a very high sampling frequency because no upper bound frequency such as the buoyancy frequency for gravity waves delimits the acoustic–gravity wave propagation frequency domain.

d. Implementation

In this section we discuss how to implement the model described above, which can be run for most cases on a standard (2009) personal computer. The first thing to consider is the domain spatial dimension and resolution. Since the result of the 3D-IDFT on a finite spectral wave field is periodic, the spatial domain must be large enough to prevent one side of the studied field to superimpose upon its other side after propagation of the studied phenomenon. If ground reflection is taken into account, the size of the spatial wave field must also be doubled in the z direction. In this case, the wave field propagates for negative altitudes and the ground reflection is accounted for at the end of the propagation process. Each component is reflected, modified according to Eq. (12), and added to the incident field. Spatial resolution mainly depends on the source spectral components. It also relies on the distance between (synthetic) recording points, which can simulate, for example, a microbarograph network.

The model can be used to investigate the evolution of any real or complex-valued pressure fluctuation field. In the case of a real-valued initial field, no information is known about the wave field direction of propagation. When calculating the 3D-DFT, energy is evenly split between opposite directions of propagation and the spectral wave field is the sum of two complex conjugate parts of positive and negative wavenumbers. At this stage, if necessary, directions of propagation can be specified. For each pair of conjugate elements, the one that does not correspond to the direction of propagation can be removed while the amplitude of the opposite one is doubled. The consequence of this filtering operation is to get the phase of the spatial field when applying the 3D-IDFT to the resultant spectral field (Bracewell 1999).

Once the initial spectral wave field is obtained, the next step is to calculate the value of the angular frequency ω in the same spectral domain as the wave field 3D-DFT. From this angular frequency field we can deduce the phase shift that each monochromatic wave undergoes over the considered time interval. This phase shift is then included in an imaginary exponential term that is multiplied by the 3D-DFT of the initial field [Eq. (14)]. The wave field can then be propagated on any time interval until the first source interferes. If the source needs to be discretized, condition (19) must be verified and source effect samples are successively added in the spectral domain according to Eq. (17). Since source samples need to be inserted in the spectral model, there is no need to come back to the spatial domain unless pressure fluctuations need to be known. In this case the 3D-IDFT of the spectral field must be calculated.

Once the final normalized pressure fluctuation field is obtained, the reflection at the ground surface is calculated in the spectral domain. This is done by taking the symmetric field about the plane $m = 0$, multiplying it by the proper complex coefficient [Eq. (12)] and adding it to the original spectral field. Note that the wave field amplitudes obtained far from the ground must be interpreted cautiously because wave amplitude exponentially increases with height and the linear characteristic of the model discards all nonlinear processes such as wave breaking or interactions. Complex amplitudes of other wave perturbation variables such as wind velocity components or potential temperature can then be obtained from the 3D-DFT of the normalized pressure fluctuation field (including reflection) using gravity wave polarization relations. Finally, the influence of density stratification variations is taken into account for each gravity wave perturbation variable. In the case of the pressure, for example, fluctuations are deduced from normalized pressure fluctuations using Eq. (15). As seen in section 2a, a realistic atmospheric density profile can be used for this operation.

3. Validation: St. Andrew's cross

The purpose of this section is to retrieve a classical result of internal gravity wave beams produced by a time-monochromatic localized disturbance in a stably stratified fluid (e.g., Lighthill 1978; Voisin 1991). This case is often explored through the Boussinesq approximation, which consists of not taking into account density variations in fundamental fluid equations except for the calculation of buoyancy forces. It is a quite fair approximation for most wave vectors and is often used to simplify calculations. It is the same as considering $c_S \to \infty$ in the dispersion relation (3) (Fritts and Alexander 2003).

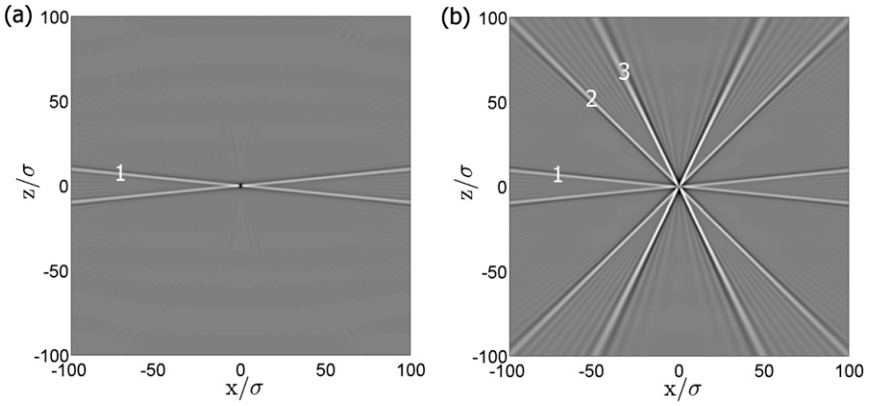

FIG. 1. Pressure fluctuation field after four oscillations at a frequency $\omega_0 = 2.10^{-3}$ rad s^{-1} of a normalized pressure fluctuation monochromatic Gaussian monopole for two different sampling frequencies (a) $\omega_{Sa} = 16\omega_0$ and (b) $\omega_{Sb} = 8\omega_0$. Axes are normalized to σ, the Gaussian standard deviation. Numbers 1, 2, and 3 correspond to angles α_0, α_{1-}, and α_{1+}, respectively.

The influence of the density scale height in the dispersion relation is also neglected, a valid approximation for waves with vertical wavelengths smaller than the density scale height ($m^2 \gg 1/4H^2$). In this case of constant density, the normalized pressure fluctuation is simply the pressure fluctuation. Considering no background wind and ignoring rotational effects ($f \to 0$), the dispersion relation for a two-dimensional fluid becomes

$$\omega = \frac{Nk}{\sqrt{k^2 + m^2}}. \tag{21}$$

Boussinesq waves produced by a localized time-monochromatic disturbance are known to propagate inside beams, which develop around a St. Andrew's cross in two dimensions (e.g., Lighthill 1978; Voisin 1991). For a source oscillating at the angular frequency ω_0 with $0 < \omega_0 < N$, the energy is radiated around an angle α to the vertical such that

$$\alpha = \arccos\left(\frac{\omega_0}{N}\right). \tag{22}$$

We here consider a real-valued normalized pressure fluctuation Gaussian forcing F_ϕ oscillating at the angular frequency ω_0:

$$F_\phi(x, z, t) = A\omega_0 H(t) \exp\left(-\frac{x^2 + z^2}{2\sigma^2}\right) \cos(\omega_0 t), \tag{23}$$

with $H(t)$ being the Heaviside step function, A the pressure monopole amplitude, and σ the standard deviation, which is the spatial measure of the source size. The source is time discretized with a constant angular sampling frequency ω_S. Source effect samples are calculated using Eq. (16):

$$s_n(x, z) = 2A \exp\left(-\frac{x^2 + z^2}{2\sigma^2}\right) \sin\left(\pi \frac{\omega_0}{\omega_S}\right) \cos\left(2\pi n \frac{\omega_0}{\omega_S}\right) \tag{24}$$

Figure 1 represents the real part of the normalized pressure fluctuation field after four oscillations of the source for two different sampling frequencies $\omega_{Sa} = 16\omega_0$ and $\omega_{Sb} = 8\omega_0$ with $\omega_0 = 2.10^{-3}$ rad s^{-1}, $N = 2.10^{-2}$ rad s^{-1}, and $\sigma = 5$. The grid dimension is 2048×2048 but only the central 512×512 part of the grid is shown in Fig. 1. On both figures we can see the expected St. Andrew's cross (marked 1) radiated around $\alpha = \arccos(\omega_0/N) \approx 84°$ with the vertical. In Fig. 1a the sampling frequency ω_S is higher that the buoyancy frequency N; consequently, the model sees the source as continuous and only one cross appears. In Fig. 1b condition (20) is not satisfied and extra crosses (marked 2 and 3) generated by the succession of impulsive source at a frequency lower than the buoyancy frequency also propagate. The link between the appearance of these extra waves and the choice of the sampling frequency is discussed in the appendix. Provided condition (19) is met, the classical asymptotic result of internal gravity wave beams produced by a time-monochromatic disturbance is retrieved. Note that this model can also be used to follow the wave field temporal evolution and to visualize the group velocity of the wave beams, for example.

4. Application: Total solar eclipse

a. Asymptotic response

We now consider a geophysical situation that requires the use of the fully compressible dispersion relation for inertia–gravity waves because of the large time and

space scales involved. The absorption of solar ultraviolet radiations by the ozone layer during a solar eclipse is reduced or even stopped in the totality path. This creates a cooling region in the atmosphere, which acts as a continuous source of internal gravity waves and produces a large-scale bow wave as the eclipse shadow moves on the earth's surface at supersonic speed (Chimonas and Hines 1970). Chimonas (1970) proposed an analytical theory to estimate pressure variations induced by the cooling of the ozone layer. He estimated pressure variations just over 1 Pa at the ground level for the total solar eclipse of 7 March 1970. Two decades later, Fritts and Luo (1993) studied the asymptotic response to an average stratospheric thermal forcing traveling through the atmosphere with a constant velocity. They numerically solved fundamental fluid equations under the pseudoincompressible approximation (Durran 1989) in the eclipse shadow referential. To compare our solutions with these previous models, we also consider an average stratospheric thermal forcing F_T traveling through the atmosphere with a constant horizontal velocity V. The constant source velocity can be taken into account by considering a stationary source in an atmosphere with a constant zonal background wind $\overline{u} = -V$. The source is stationary; thus, its 3D-DFT only needs to be calculated once. Using the ideal gas state equation, normalized pressure fluctuation samples are given by

$$s(x, y, z) = \rho_0 R_M e^{-(z/2H)} \int_{-\Delta t/2}^{\Delta t/2} F_T(x, y, z)\, dt, \quad (25)$$

with Δt being the source effects integration time, R_M the specific gas constant, and F_T the thermal forcing approximated by Fritts and Luo (1993) to a three-dimensional Gaussian:

$$F_T(x, y, z) = Q \exp\left[-\frac{(x^2 + y^2)}{2\sigma_r^2} - \frac{(z - z_0)^2}{2\sigma_z^2}\right], \quad (26)$$

with $|Q| = 12$ K day^{-1}, $\sigma_r = 1460$ km, $\sigma_z = 10$ km, and $z_0 = 50$ km. Since the occultation of the Sun induces a temperature decrease, we use a negative thermal forcing amplitude $Q = -12$ K day^{-1}. Figure 2 represents the asymptotic solutions for pressure variations p' at the ground level. Contour intervals are 0.3 Pa. Zero and positive contours are solid and negative contours are dashed. The outer and inner shaded disks contain 99% and 67% of the source effects, respectively. Atmospheric parameters, representative of the stratopause, are the same as those used by Fritts and Luo (1993), that is, a mean temperature $T = 266$ K, a buoyancy frequency $N = 0.02$ rad s^{-1}, and a density scale height $H = 7.8$ km. The shadow velocity $V = 740$ m s^{-1} is also identical. Spatial resolution is set to 50 km horizontally and 1 km vertically. The source discretization time $\Delta t = 1$ min is in agreement with condition (19). The grid dimension is $2048 \times 1024 \times 256$. The asymptotic solution is reached after 40 h (simulation time), when the field does not evolve anymore in the studied region.

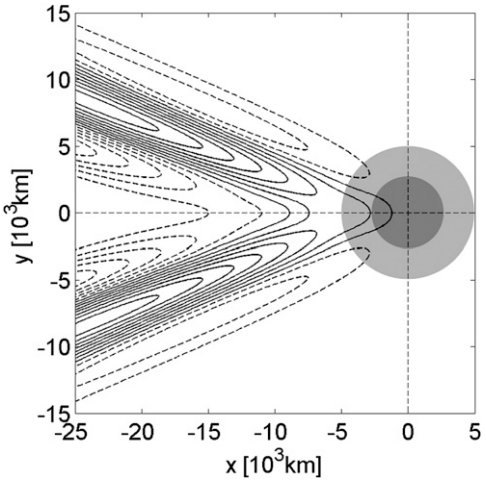

FIG. 2. Asymptotic pressure perturbation p' induced at the ground level by an eclipse moving through the atmosphere with constant velocity. Zero and positive contours are solid; negative contours are dashed. Contour intervals are 0.3 Pa. The outer and inner shaded disks contain 99% and 67% of the source effects, respectively.

A large-scale bow wave similar to the one predicted by Chimonas and Hines (1970) is shown in Fig. 2. The pressure variation, just over 2 Pa, is as high as twice the one predicted by Chimonas (1970). This is because we have considered ground reflection in our model. Fritts and Luo (1993) only presented their solutions for wave perturbation variables above 80 km. They did not show results for pressure fluctuations; thus, to compare our solutions with theirs, we need to calculate the amplitudes of meridional v' and vertical w' velocities perturbation using the corresponding polarization relations:

$$\tilde{v} = \left(\frac{\hat{\omega} l - ifk}{\hat{\omega}^2 - f^2}\right)\tilde{p}, \quad (27)$$

$$\tilde{w} = -\frac{\hat{\omega}(m - i\Gamma)}{N^2 - \hat{\omega}^2}\tilde{p}. \quad (28)$$

Figure 3 shows our asymptotic solutions for the vertical w' and meridional v' velocity perturbations at an altitude of 80 km. Contour intervals are 0.1 cm s^{-1} for w' and 15 cm s^{-1} for v'. Zero and positive contours are solid; negative contours are dashed. The shaded area represents the spatial domain for which Fritts and Luo

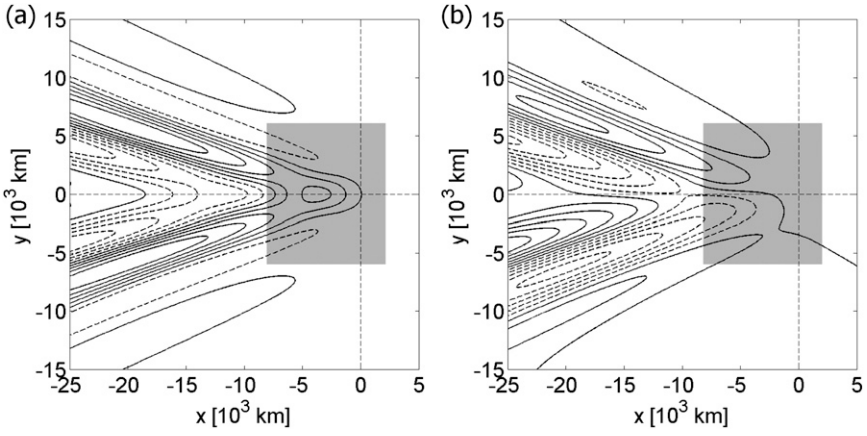

FIG. 3. Asymptotic (a) vertical w' and (b) meridional v' velocity perturbations induced at an altitude of 80 km by an eclipse moving through the atmosphere with constant velocity. Contour intervals are 0.1 cm s^{-1} for w' and 15 cm s^{-1} for v'. Zero and positive contours are solid; negative contours are dashed. The shaded area represents the spatial domain for which Fritts and Luo (1993) calculated their numerical solutions.

(1993) calculated their numerical solutions. To compare our fluctuation amplitudes with Fritts and Luo's (1993), we did not take into account the reflection at the ground.

We can see that the bow-wave shape and intensity are fairly similar to Fritts and Luo (1993) solutions. Differences between the solutions can be explained through two main considerations. First, Fritts and Luo (1993) considered the pseudoincompressible approximation when resolving fundamental fluid equations whereas we have used the fully compressible dispersion relation. The pseudoincompressible approximation was proposed by Durran (1989) to filter out sound waves in fundamental fluid equations while conserving total kinetic and anelastic dry static energy. It only requires modifications in the mass continuity equation, in contrast to other anelastic approximations. However, Eckermann et al. (2007) stressed several weaknesses in this approximation. They showed that this approximation allows a greater range of harmonic pairs ($\hat{\omega}$, $\mathbf{k}$) to be freely propagating gravity waves. The generation of internal gravity waves is particularly overestimated for low-frequency waves, and internal gravity waves are allowed to propagate vertically at supersonic phase speeds. This can explain why Fritts and Luo's (1993) solutions are spatially ahead of our solutions in the zonal direction. The second point is that Fritts and Luo (1993) did not take into account the earth's rotation. According to the fully compressible dispersion relation (3), we can see that rotational terms are not negligible for low-frequency gravity waves such as those produced by the eclipse shadow. In our simulation, we have chosen a Coriolis parameter $f = 1.10^{-4}$ rad s^{-1}, which corresponds to a midlatitude trajectory. The influence of rotational effects is particularly visible on the absolute meridional velocity wave field, which is not symmetrical with respect to the x axis.

b. Transient response

The asymptotic solution, obtained in the previous section, was reached after propagating the eclipse shadow for 40 h. However, solar eclipses last on average only a couple hours at the earth's surface, which is clearly not long enough to allow the asymptotic bow wave to be formed. The model described in this paper is designed to reproduce spatial and temporal evolution of source effects. The beginning and the end of the eclipse can therefore be taken into account, as well as variations of shadow trajectory and velocity. Eckermann et al. (2007) proposed a nonasymptotic solution for the thermal forcing due to the 4 December 2002 solar eclipse using a high-altitude global numerical weather prediction model. Shadow trajectory, duration, and velocity are parameters that significantly vary from one eclipse to another. Thus, in order to compare our solutions with Eckermann et al. (2007), we focus our analysis on the same solar eclipse and use the parameters provided by Espenak and Anderson (2001).

The total eclipse duration is approximately 3 h 21 min and the shadow velocity reaches a minimum of 670 m s^{-1} at eclipse maximum (Eckermann et al. 2007, their Fig. 2). Unlike the asymptotic case, the simulation is run in the terrestrial reference frame and the ground reflection is taken into account. The shadow position is therefore updated at each addition of source effect sample. The source velocity is also modified all along the eclipse path by changing the time interval between the insertions of two consecutive source samples. The instantaneous

sampling frequency constantly varies because the shadow velocity does. To ensure that condition (19) is met all along the eclipse path, the horizontal spatial resolution is set to 25 km. Since the propagation is on a smaller time scale (compared to the asymptotic case), we can consider a smaller grid dimension ($1024 \times 1024 \times 256$).

To get a first approximation, the shadow shape and the cooling rate profile are assumed to be constant. For the shadow shape, we refer to Eckermann et al. (2007), who demonstrated that the solar intensity reduction mainly depends on disk geometry and solar limb darkening for wavelengths responsible for ozone heating. They proposed a normalized solar intensity reduction function E_{UV} depending on the eclipse magnitude E_M. They showed that the eclipse magnitude E_M varies approximately linearly from the central eclipse region to the penumbral perimeter except during the beginning and end phases of the eclipse. However, the contribution of these two extreme phases to the atmospheric cooling is low because of the high velocity of the eclipse shadow during these phases. For the same reason, the shadow shape, which is elongated and truncated by the terminator during the beginning and the end phase of the eclipse, is assumed to be a perfect disk all along the eclipse path. The eclipse magnitude E_M at the time t_n can therefore be approximated in the shadow region by the function μ_n defined as

$$\mu_n(x, y) = (E_M)_{\max} - \frac{\sqrt{(x - x_n)^2 + (y - y_n)^2}}{r_p}, \qquad (29)$$

where (x_n, y_n) is the center of the penumbra disk and r_p its radius, and $(E_M)_{\max} = 1.02437$ for the 4 December 2002 eclipse (Espenak and Anderson 2001). The source intensity mainly depends on two criteria: ozone concentration and sun zenith angle. The central path of the 4 December 2002 total eclipse is bounded between 4°S and 44°S in latitude. According to Eckermann et al. (2007, their Figs. 1, 3 and 6), ozone concentration does not vary too much horizontally between these latitudes and solar zenith angle mainly influences the heating rate of the beginning and the ending phases of the eclipse. We thus consider a constant Gaussian vertical heating rate. The thermal forcing F_{Tn} at the time t_n can therefore be written as

$$F_{\mathrm{Tn}}(x, y, z) = QE_{UV}(\mu_n) \exp\left[-\frac{(z - z_0)^2}{2\sigma_z^2}\right], \qquad (30)$$

with $z_0 = 50$ km, $\sigma_z = 10$ km, and $Q = -20$ K day^{-1}. Atmospheric parameters remain the same as for the asymptotic simulation (section 4a) except the Coriolis parameter $f = -5.10^{-5}$ rad s^{-1}. Figure 4 shows the vertical velocity wave field at 1000 UTC for an altitude of 50 km. The vertical velocity is calculated from the pressure using the polarization equation (28). Scales and units are given in the color bar and the green dashed line shows the path of the umbral shadow from the beginning to the end of the total eclipse. The solution is projected on a world map to be compared with Eckermann et al. (2007, their Fig. 13c). The V-shaped wave field is very similar to one produced by the high-altitude global numerical weather prediction model used by Eckermann et al. (2007). Vertical velocity maximal amplitude is also of the same order of magnitude. The small differences apparent at the lowest latitudes for example, probably occur because our model does not perform calculations in spherical coordinates and cannot consider wind or buoyancy frequency profiles. The positive wave field over southern Africa is also more intense in Eckermann et al.'s (2007) solution. This might be due to the fact that we considered a constant shape and intensity for the solar intensity reduction, not fully representative of the beginning and the ending phases of the eclipse. However, the model is designed to take into account source shape and intensity variations. Thus, the influence of ozone concentration and sun zenith angle on the thermal forcing term could be integrated in further simulations. Despite the approximations used in defining the source our model provides results in good agreement with those from Eckermann et al. (2007). This clearly demonstrates that internal gravity waves are the main atmospheric process responsible for propagating the perturbation induced by a solar eclipse in the stratosphere.

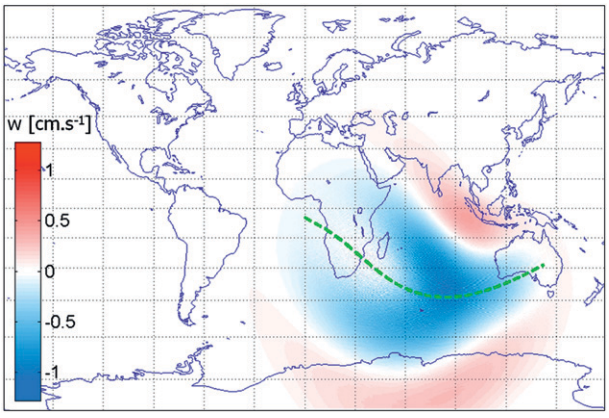

FIG. 4. Vertical velocity wave field at 1000 UTC 4 Dec 2002 for an altitude of 50 km. Scales and units are given in the color bar and the green dashed line shows the path of the umbral shadow from the beginning to the end of the total eclipse.

5. Discussion and prospects

In this article, we have presented a three-dimensional linear spectral numerical model able to propagate gravity

wave perturbations in a stably stratified atmosphere. The linearization of fundamental fluid equations discards all nonlinear processes such as wave breaking or interactions. The spectral implementation also excludes situations involving spatial variations of background wind or buoyancy frequency. Despites these limitations, the model offers definite advantages compared with other linear models (e.g., Lighthill 1978; Fritts and Luo 1992). First, it takes into account the fully compressible gravity wave dispersion relation. In the case of the asymptotic response to the ozone layer cooling during a solar eclipse, our solutions look more realistic than those of Fritts and Luo (1993), who had to go through the pseudoincompressible approximation to resolve the fundamental fluids equations. Furthermore, the model can take into account spatially and temporally evolving sources. In the case of the 4 December 2002 eclipse, the beginning and the end of the eclipse are considered, as well as variations in source trajectory and velocity. The transient response simulated with our model is very similar in shape and intensity to the one obtained with Eckermann et al.'s (2007) high-altitude global numerical weather prediction model. This means that our model can quickly provide, in terms of programming and calculation time, a good approximation of the wave field produced by a solar eclipse. It can therefore be used to produce synthetic fluctuations that can be compared to observations or can facilitate measurement campaign planning.

While not demonstrated here, the variation of source shape and intensity could be integrated within our model. The investigation of internal gravity waves produced during a solar eclipse could also be expanded to other potential sources. Chimonas (1970) mentioned that the absorption of infrared radiation by tropospheric water vapor could produce a bow wave similar to that resulting from the ozone. Because of the linearity of the model tropospheric and stratospheric simulations can be conducted independently and simply added afterward. The influence of both sources on ground pressure variations can then be evaluated. These are features that will be presented in a future paper. They will be applied to characteristics of the 1 August 2008 eclipse and pressure fluctuations simulated at the ground surface will be compared to existing microbarograph records.

APPENDIX

Sampling Frequency Criteria

The purpose of this appendix is to explain and characterize the extra crosses generated by a time-monochromatic localized disturbance sampled with a frequency lower than the buoyancy frequency (section 3). The 3D-DFT of the normalized pressure fluctuation wave field ϕ exposed to the forcing F_ϕ described in Eq. (23) can be written at an arbitrary time t_M as

$$\hat{\phi}_{k,m}(t_M) = \sum_{n=0}^{M-1} \hat{s}_n(k,m) e^{-2i\pi(M-n)(\omega/\omega_S)}. \quad \text{(A1)}$$

According to the expression of source effects samples s_n [Eq. (24)], Eq. (A1) can be rearranged in the form

$$\hat{\phi}_{k,m}(t_M) = B_{k,m} \sum_{n=0}^{M-1} \cos\left(2\pi n \frac{\omega_0}{\omega_S}\right) e^{2in\pi(\omega/\omega_S)}, \quad \text{(A2)}$$

with

$$B_{k,m} = 2A\sigma^2 \sin\left(\frac{\pi\omega_0}{\omega_S}\right) \times \exp\left[-\frac{\sigma^2}{2}(k^2+m^2) - 2i\pi M \frac{\omega}{\omega_S}\right]. \quad \text{(A3)}$$

Developing Eq. (A2) with complex notations and recognizing geometric progression forms, it follows that the only monochromatic waves that see their amplitudes continuously increasing are those with angular frequencies equal to

$$\omega = \omega_{j\pm} = j\omega_S \pm \omega_0, \quad \text{(A4)}$$

with j being an integer. In our case ω is positive; thus j is a natural integer. If $\omega_S > N$, the only solution inside of the gravity wave frequency propagation domain is $\omega = \omega_0$; thus, the wave field is similar to the one that would be generated by the corresponding continuous source. Otherwise a whole set of frequencies, which would depend on the sampling frequency and would not be excited by the corresponding continuous source, is the solution of Eq. (A4). The energy of these extra waves is radiated around angles $\alpha_{j\pm}$, defined as

$$\alpha_{j\pm} = \arccos\left(\frac{\omega_{j\pm}}{N}\right), \quad \text{(A5)}$$

with $\omega_{j\pm} \leq N$. This corresponds to the two extra crosses displayed in Fig. 1b around angles $\alpha_{1-} = \arccos[(\omega_S - \omega_0)/N] \approx 46°$ (cross 2) and $\alpha_{1+} = \arccos[(\omega_S + \omega_0)/N] \approx 34°$ (cross 3).

REFERENCES

Bracewell, R., 1999: *The Fourier Transform and Its Applications*. 3rd ed. McGraw-Hill, 640 pp.

Broutman, D., and J. W. Rottman, 2004: A simplified Fourier method for computing the internal wavefield generated by an oscillating source in a horizontally moving, depth-dependent background. *Phys. Fluids,* **16,** 3682–3689.

——, ——, and S. D. Eckermann, 2003: A simplified Fourier method for nonhydrostatic mountain waves. *J. Atmos. Sci.,* **60,** 2686–2696.

Chimonas, G., 1970: Internal gravity-wave motions induced in the earth's atmosphere by a solar eclipse. *J. Geophys. Res.,* **75,** 5545–5551.

——, and C. O. Hines, 1970: Atmospheric gravity waves induced by a solar eclipse. *J. Geophys. Res.,* **75,** 875–876.

Durran, D. R., 1989: Improving the anelastic approximation. *J. Atmos. Sci.,* **46,** 1453–1461.

Eckermann, S. D., D. Broutman, M. T. Stollberg, J. Ma, J. P. McCormack, and T. F. Hogan, 2007: Atmospheric effects of the total solar eclipse of 4 December 2002 simulated with a high-altitude global model. *J. Geophys. Res.,* **112,** D14105, doi:10.1029/2006JD007880.

Espenak, F., and J. Anderson, 2001: Total solar eclipse of 2002 December 04. NASA Tech. Paper NASA/TP-2001-209990, 86 pp. [Available online at http://umbra.nascom.nasa.gov/pub/eclipse/021204/TP2001209990.pdf.]

Fovell, R., D. Durran, and J. R. Holton, 1992: Numerical simulations of convectively generated stratospheric gravity waves. *J. Atmos. Sci.,* **49,** 1427–1442.

Fritts, D. C., and Z. Luo, 1992: Gravity wave excitation by geostrophic adjustment of the jet stream. Part I: Two-dimensional forcing. *J. Atmos. Sci.,* **49,** 681–697.

——, and ——, 1993: Gravity-wave forcing in the middle atmosphere due to reduced ozone heating during a solar eclipse. *J. Geophys. Res.,* **98,** 3011–3021.

——, and M. J. Alexander, 2003: Gravity wave dynamics and effects in the middle atmosphere. *Rev. Geophys.,* **41,** 1003, doi:10.1029/2001RG000106.

Gossard, E., and W. Hooke, 1975: *Waves in the Atmosphere.* Elsevier, 456 pp.

Hauf, T., U. Finke, J. Neisser, G. Gull, and J. G. Stangenberg, 1996: A ground-based network for atmospheric pressure fluctuations. *J. Atmos. Oceanic Technol.,* **13,** 1001–1023.

Lighthill, J., 1978: *Waves in Fluids*. Cambridge University Press, 504 pp.

Marks, C. J., and S. D. Eckermann, 1995: A three-dimensional nonhydrostatic ray-tracing model for gravity waves: Formulation and preliminary results for the middle atmosphere. *J. Atmos. Sci.,* **52,** 1959–1984.

Rees, J. M., J. C. W. Denholm-Price, J. C. King, and P. S. Anderson, 2000: A climatological study of internal gravity waves in the atmospheric boundary layer overlying the Brunt Ice Shelf, Antarctica. *J. Atmos. Sci.,* **57,** 511–526.

Thorpe, S. A., 1987: On the reflection of a train of finite-amplitude internal waves from a uniform slope. *J. Fluid Mech.,* **178,** 279–302.

Voisin, B., 1991: Internal wave generation in uniformly stratified fluids. Part 1: Green's function and point sources. *J. Fluid Mech.,* **231,** 439–480.

——, 1994: Internal wave generation in uniformly stratified fluids. Part 2: Moving point sources. *J. Fluid Mech.,* **261,** 333–374.